Check for updates

Crystal genes in a marginal glass-forming system of Ni$_{50}$Zr$_{50}$

T. Q. Wen,[ab] L. Tang,[bc] Y. Sun, [ID][b] K. M. Ho,[bd] C. Z. Wang*[bd] and N. Wang [ID] *[a]

The marginal glass-forming ability (GFA) of a binary Ni–Zr system is an issue to be explained considering numerous bulk metallic glasses (BMGs) found in a Cu–Zr system. Using molecular dynamics, the structures and dynamics of Ni$_{50}$Zr$_{50}$ metallic liquid and glass are investigated at the atomistic level. To achieve a well-relaxed glassy sample, a sub-T_g annealing method is applied and the final sample is closer to the experiments than the models prepared by continuous cooling. With the state-of-the-art structural analysis tools such as cluster alignment and pair-wise alignment methods, two glass-forming motifs with some mixed traits of a metastable B2 crystalline phase and a crystalline Ni-centered B33 motif are found to be dominant in the undercooled liquid and glass samples. A new chemical order characterization on each short-range order (SRO) structure is accomplished based on the cluster alignment method. The significant amount of the crystalline motif and the few icosahedra in the glassy sample deteriorate the GFA.

1. Introduction

Recently, it has been found that bulk metallic glass (BMG) can be produced in a binary Cu–Zr system at several compositions, *e.g.*, Cu$_{65}$Zr$_{35}$,[1–3] Cu$_{60}$Zr$_{40}$,[1,4] Cu$_{56}$Zr$_{44}$,[3] Cu$_{50}$Zr$_{50}$,[3,5] and Cu$_{45}$Zr$_{55}$.[4,6] For example, Wang *et al.*[2] found that BMG with a diameter of 2 mm could be fabricated by copper mold casting at Cu$_{64.5}$Zr$_{35.5}$ with a composition accuracy of 0.5 at%. Li *et al.*[3] measured the critical thickness of Cu–Zr wedge-shaped molds for glass formation and found that the three maxima are 1.14 ± 0.04 mm at Cu$_{50}$Zr$_{50}$, 1.02 ± 0.04 mm at Cu$_{56}$Zr$_{44}$, and 1.14 ± 0.04 mm at Cu$_{64}$Zr$_{36}$, which match with the three minima in the density change upon crystallization. Besides, interpenetrated icosahedra (ICO) networks have been shown in Cu–Zr systems by theoretical simulations.[7–9] From the periodic table, nickel and copper are neighbors and have similar atomic sizes. The glass-forming composition range of Ni–Zr alloy is predicted to be between 10 and 80 at% Zr by López *et al.*[10] and 20 and 80 at% Zr by Yang *et al.*,[11] respectively, which is consistent with the mechanical alloying experimental results of 17–76 at% Zr.[12] However, BMG has not yet been observed in the Ni–Zr system and only a very small size of glassy samples could

be made from mechanical alloying,[12] melt spinning,[13] splat quenching,[14] *etc.* The glass-forming ability (GFA) in nature is determined by microscopic interatomic interactions and many studies on the atomistic structures revealed that the microscopic short-to-medium range orders have strong influences on the macroscopic properties of the metallic glasses (MGs).[15–19] For example, Kim *et al.*[19] carried out a comparative study of Cu$_{50}$Zr$_{50}$ and Cu$_{47.5}$Zr$_{47.5}$Al$_5$ systems and found that the addition of a minor amount of Al element helps in developing a better medium-range order (MRO) and thus enhances the GFA and the strength of the material. On the other hand, in a binary Al–Sm metallic glass system, local clusters with a "3661" packing motif have been recently identified to be the dominant short-range order (SRO) but they do not form an interpenetrating network, which explains the marginal GFA in the Al–Sm system.[18] From these examples, we can see that the weak GFA of the Ni–Zr system could be traced back to the underlying microscopic structural and chemical orders in its undercooled and amorphous states.

From the perspective of microscopic structural and chemical orders, the glass-forming process involves competitions between the glass-forming motifs like ICO and the crystalline ones (*e.g.* FCC, BCC, HCP, *etc.*). From the phase diagram of Ni–Zr alloy systems,[20] the simple crystalline phase, B33, is the most stable state at the composition of 50 at% Zr. As a result, it is of interest to investigate the structural basis which hinders the formation of BMG in the Ni$_{50}$Zr$_{50}$ system from the perspective of the competition between different structural and chemical SROs in deeply undercooled liquids.

So far studies of the atomistic structures of undercooled liquid and glass of the Ni–Zr system at the composition of

[a] MOE Key Laboratory of Materials Physics and Chemistry under Extraordinary Conditions, School of Natural and Applied Sciences, Northwestern Polytechnical University, Xi'an 710072, China. E-mail: nan.wang@nwpu.edu.cn

[b] Ames Laboratory-USDOE, Iowa State University, Ames, Iowa 50011, USA. E-mail: wangcz@ameslab.gov

[c] Department of Applied Physics, College of Science, Zhejiang University of Technology, Hangzhou, 310023, China

[d] Department of Physics and Astronomy, Iowa State University, Ames, Iowa 50011, USA

50 at% Zr are still very limited. Yang *et al.*[21] carried out molecular dynamics (MD) and Monte Carlo simulations and found out that ICO or distorted ICO cover a dominant fraction at Ni_xZr_{100-x} (x = 35, 50, and 65) MGs. From this study, however, the characteristic of $Ni_{50}Zr_{50}$ being a marginal glass former still cannot be explained. Recently, Wilson and Mendelev[22] developed an accurate semi-empirical embedded-atom method (EAM) potential of the Finnis–Sinclair (FS) type[23] to study the solid–liquid interface in the $Ni_{50}Zr_{50}$ alloy. The accuracy and efficiency of this EAM potential provide us with a reliable tool to perform extensive MD simulation to investigate the microscopic structural and chemical orders in the deeply undercooled and glassy $Ni_{50}Zr_{50}$ systems.

One widely used method to obtain a glassy sample in both experiment and theoretical simulation is rapid quenching.[24–26] If the cooling rate is fast enough, the formation of crystalline phases is restrained and the glassy sample could then be produced. Phase selection is significantly dependent on the cooling rate and the challenge for MD simulation is that the cooling rate (normally faster than 10^9 K s^{-1}) is much higher than that can be achieved in experiments (10^3–10^6 K s^{-1}) because of the time scale in MD simulations. Recently, a sub-T_g annealing method, which anneals and relaxes the atomistic structures below but close to the glass transition temperature (T_g), shows the ability to lower the effective cooling rate and achieve lower-energy glassy samples.[18,27,28]

In this paper, we performed MD simulations to investigate the GFA of $Ni_{50}Zr_{50}$ using the EAM potential developed in ref. 22. We employed the sub-T_g annealing method to generate well-relaxed $Ni_{50}Zr_{50}$ glassy samples with an effective cooling rate of about 4.47×10^8 K s^{-1}. The cluster alignment method[29–31] and the pair-wise alignment[32] are then applied to characterize the SRO motifs and explore the possible competition between the crystal motif and glass-forming SROs in the glass samples. The Ni-centered B33 crystal motif from crystals and two other glass-forming motifs from pair-wise alignment are found to be the abundant SROs in the glassy samples. The chemical order of these motifs are then determined in detail. The chemical order of the Ni-centered B33 motif is the same as that from the crystalline phase and the glass-forming motifs are found to have some characteristics of a B2 crystalline motif. The abundance of a Ni-centered B33 crystal motif and the low fraction of ICO contribute to the inferior GFA of the system. We also study the dynamical behavior of the system at the atomic level and establish the close relation between the local structure order and dynamics in the system.

2. Simulation details and analysis methods

MD simulations of the $Ni_{50}Zr_{50}$ intermetallic alloy are performed by using the LAMMPS package[33] and a semi-empirical EAM potential of the FS type.[23] The EAM potential is a semi-empirical many-body potential which is particularly appropriate for metallic systems. The potential energy in FS-type takes the following form:

$$U = \sum_{i=1}^{N-1} \sum_{j=i+1}^{N} \varphi_{\alpha_i\alpha_j}(r_{ij}) + \sum_{i=1}^{N} \Phi_{\alpha_i}(\rho_i), \quad (1)$$

where N is the number of atoms, $r_{i,j}$ is the separation between atoms i and j, $\varphi_{\alpha_i\alpha_j}(r)$ is the pairwise potential, $\Phi_{\alpha_i}(\rho)$ is the embedding energy function, and

$$\rho_i = \sum_j \psi_{\alpha_i\alpha_j}(r_{ij}), \quad (2)$$

where $\psi_{\alpha_i\alpha_j}(r)$ are density functions and α_i is the element type of atom i. The potential parameters used in the present simulations are taken from ref. 22.

The isothermal–isobaric ensemble (*NPT, N* = 5000 atoms, *P* = 0) and a Nose–Hoover thermostat are used throughout the sample preparation. The periodic boundary conditions are applied in all the three directions and the time step for integration is 2.5 fs through the whole process. The liquid sample containing 2500 Ni atoms and 2500 Zr atoms is initially equilibrated at 2000 K for 5 ns (2 million steps) and then cooled down continuously to 300 K at the rate of 10^9, 10^{10}, 10^{11}, 10^{12}, and 10^{13} K s^{-1}, respectively. The simulations at the cooling rate from 10^{10} to 10^{13} K s^{-1} are repeated five times and that at 10^9 K s^{-1} is repeated three times by changing the initial velocity, which helps in acquiring more reliable statistics. Fig. 1 shows the change in energy with temperature at a cooling rate of 10^{10} K s^{-1}. There are obviously two regions: (1) the glass region where the energy changes slightly; (2) the high temperature region where the energy decreases considerably during quenching. The glass transition temperature T_g can be estimated from the boundary between these two regions, which is around 850 K. The sub-T_g annealing method is then applied to the 10^{10} K s^{-1} quenched sample at 800 K for 2.0 μs, followed by continuous cooling to 300 K at 10^{10} K s^{-1}. In order to eliminate the thermal vibrations on

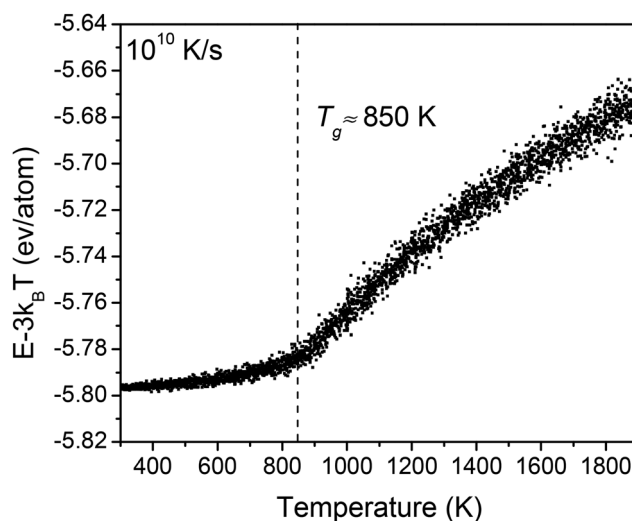**Fig. 1** Change in energy during cooling the $Ni_{50}Zr_{50}$ liquid from 2000 K to 300 K at a cooling rate of 10^{10} K s^{-1}.

atomic structures, snapshots in 500 ps are collected to calculate the averaged atomic positions at 300 K. At other temperatures, we use the inherent structures obtained by freezing the structure rapidly and the frozen structure is thus deprived of the thermal effect and used for further structural analysis.

To characterize and explore the SRO in the atomistic structure models from the MD simulations, the cluster alignment method[29–31] and the pair-wise alignment method[32] are applied to the samples. For the cluster alignment method, an alignment score is calculated to define how much the aligned cluster deviates from the structure of the template:[18]

$$f = \min_{0.80 \leq \alpha \leq 1.2} \left(\frac{1}{N} \sum_{i=1}^{N} \frac{(\vec{r}_{ic} - \alpha\vec{r}_{it})^2}{(\alpha\vec{r}_{it})^2} \right)^{1/2}, \qquad (3)$$

where N is the number of neighbor atoms in the template; $\vec{r}_{ic}$ and $\vec{r}_{it}$ are the atomic positions in the aligned cluster and template, respectively; and α is a coefficient to adapt the template's bond length. In order to achieve an optimal alignment, the range of α is chosen between 0.8 and 1.2 which helps the aligned cluster have better chance to match with the template. The smaller score indicates the higher similarity between the aligned cluster and the motif in the template.

The pair-wise alignment method[32] is based on the cluster alignment method[29–31] and the difference is that the clusters centered by the same types of atoms are aligned with each other instead of using templates. It computes a similarity matrix with $N(N-1)/2$ alignment scores for N clusters. Then the maximal clique analysis[32] is applied to sort out the dominant structure motif among the aligned clusters. For more examples of alignment methods, please also refer to ref. 7, 8, 18, 21, 27 and 28.

3. Results and discussion

3.1. The effective cooling rate

Fig. 2 shows the potential energy of the glass samples obtained from our MD simulations with different cooling rates. Lower potential energy usually corresponds to a more stable and relaxed glassy structure. A linear dependence of potential energy on the logarithm of the cooling rate can be seen for the continuously cooling samples, which is also observed in Cu–Zr[27,28] and Al–Sm[18] systems. Assuming this linear relationship between potential energy and cooling rate continues to be valid for even lower cooling rates, the glass structure obtained from sub-T_g annealing at 800 K for 2.0 µs would correspond to an effective cooling rate of 4.47×10^8 K s^{-1}. The total simulation time for continuous cooling at the rate of 4.47×10^8 K s^{-1} would be 3.8 µs. In this system, sub-T_g annealing shortens the simulation time for more than 40% compared to continuous cooling.

3.2. Partial pair correlation functions and structure factor

Fig. 3(a)–(c) show the partial pair correlation functions $g(r)$ for all the samples with different cooling rates. The split in the second peak in $g_{Ni–Ni}(r)$ and $g_{Ni–Zr}(r)$ and the broad second peak
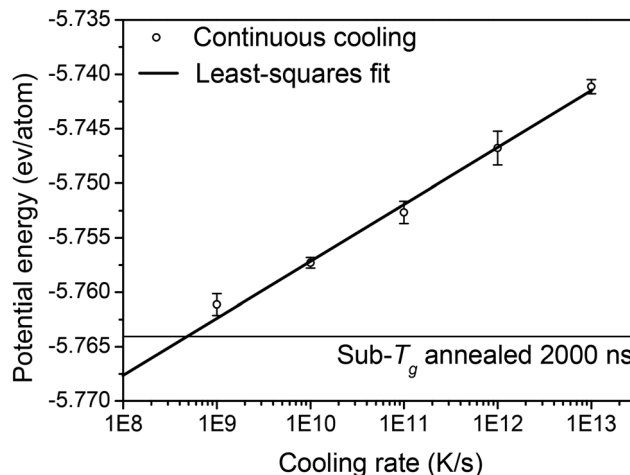

Fig. 2 Potential energy at 300 K with the change of cooling rate. The thick line indicates the least-squares fitting to a logarithm dependence for all continuously quenched samples. The effective cooling rate is equal to 4.47×10^8 K s^{-1} by sub-T_g annealing at 800 K for 2 µs.

in $g_{Zr–Zr}(r)$ suggest that the samples are in the amorphous state. For $g_{Ni–Ni}(r)$ in Fig. 3(a), the height of the first peak decreases and that of the second peak increases with decreasing cooling rate, as shown in the insets of the figure. In Fig. 3(b), both the first and the second peaks are enhanced and these two peaks shift to a longer distance for $g_{Ni–Zr}(r)$ with decreasing cooling rate. These results indicate that the atoms in the more relaxed glass sample tend to pack more tightly. In Fig. 3(c), both the first and the second peaks are enhanced but only the first peak shifts to a longer distance. In general, for $g_{Ni–Zr}(r)$ and $g_{Zr–Zr}(r)$, the peaks are enhanced with decreasing cooling rate, which indicates that the Zr center atom tends to attract more other atoms to its neighbor. On the other hand, Ni atoms tend to attract each other less and fewer Ni atoms would be in the first shell of a center Ni atom with decreasing cooling rate.

The positions of the first peaks are 2.56 Å, 2.72 Å, and 3.30 Å for $g_{Ni–Ni}(r)$, $g_{Ni–Zr}(r)$, and $g_{Zr–Zr}(r)$, respectively. Comparing $r_{Ni–Zr}$ with $r_{Ni–Ni}$ and $r_{Zr–Zr}$, we can observe a "bond shortening" phenomenon for Ni–Zr which is also found for the Cu–Al pair in Cu–Zr–Al metallic glasses.[16] Huang et al.[34] also reported that the bond length of the Ni–Zr pair is shorter than that of the Cu–Zr pair in the $Zr_2Cu_xNi_{1-x}$ ($x = 0$, 0.5, 1) system. The bond-shortening phenomenon lies in the more effective hybridization between the Zr 4d and Ni 3d bands,[35,36] consistent with the increase in Zr–Ni coordination numbers with decreasing cooling rate discussed above. Stronger attraction between Zr–Ni pairs also causes chemical ordering in the glassy sample which will be discussed in more details later in this paper.

Fig. 3(d) plots the evolution of the structure factor $S(q)$ with cooling rate and the equations used for calculating $S(q)$ from the partial $g(r)$s can be found in ref. 18. It's clear that with decreasing cooling rate, the first peak is enhanced suggesting a stronger medium-range order (MRO). From the results of potential energy, pair correlation functions and structure factor, the sub-T_g annealing process is proved to be effective to achieve a more stable and relaxed glassy sample.
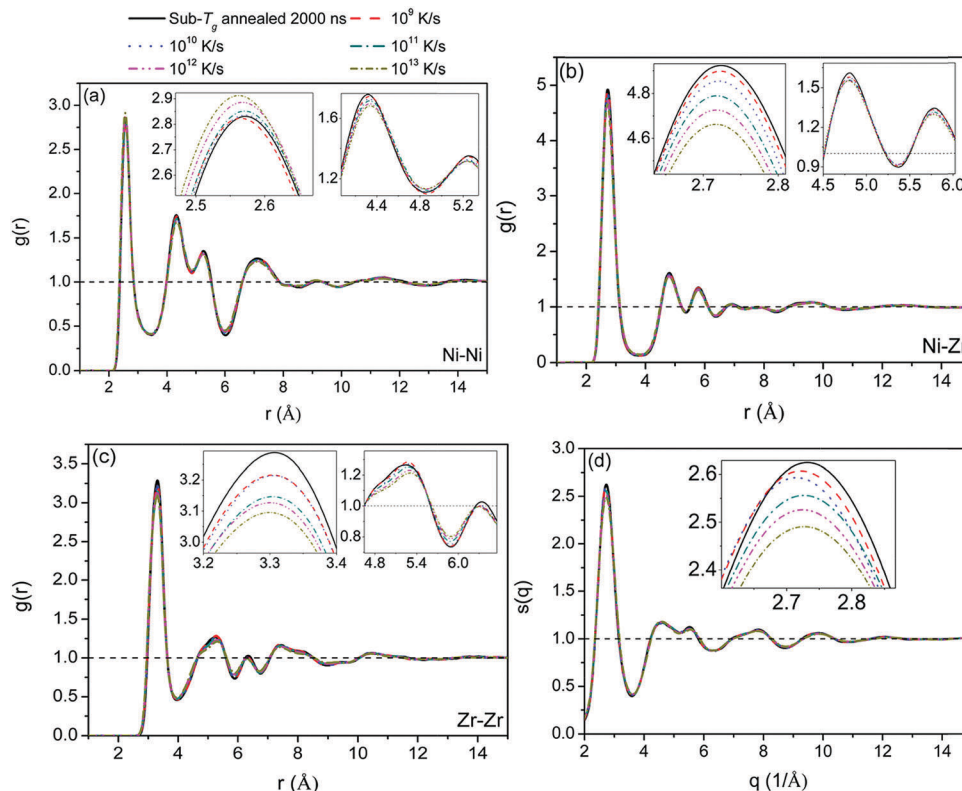
Fig. 3 (a–c) Partial pair correlation functions of Ni–Ni, Ni–Zr, and Zr–Zr at 300 K for the $Ni_{50}Zr_{50}$ glassy samples with different cooling rates. The insets show the details of the first and the second peaks. (d) The total structure factor of the glassy samples at 300 K and the inset zooms in the first peak.

3.3. Structural and chemical order

Then we turn to investigate and characterize the structural and chemical order in the glassy samples. Since the sub-T_g annealing method provides a more relaxed glassy sample corresponding to a smaller effective cooling rate, our structural and chemical order analysis below is based on this sample unless otherwise specified. From the pair correlation functions, the coordination numbers for Ni and Zr could be determined by integrating $g(r)$ up to its first minimum. The coordination number is found to be around 11 and 14.9 for Ni and Zr atoms, respectively. In order to identify the dominant local structure orders in the glass sample, we first apply pair-wise alignment[32] on the sub-T_g annealed sample to see if there is any new motif for this particular system. In Fig. 4(a) and (b), two new motifs excavated from the pair-wise alignment are shown. The red atoms are Ni and the blue ones are Zr. If a position can be occupied by either Ni or Zr, the color is green. For the motif in Fig. 4(a), there are 11 atoms around the center Ni atom and two positions have four-fold symmetry (colored in magenta), which are connected by a position with six-fold symmetry (colored in brown). The atoms in other positions form five-fold symmetry which is prevalent in ICO (Fig. 4(c)). It's similar to the Z11 with Voronoi index[37,38] $\langle 0,2,8,1 \rangle$ in ref. 39, so we call it the "Z11 motif". The Ni-centered motif in Fig. 4(b) has a coordination number of 10. When looking into the packing of the neighbor atoms, part of them show a five-fold symmetry while others are similar to the first shell of B2 (colored in orange) considering the
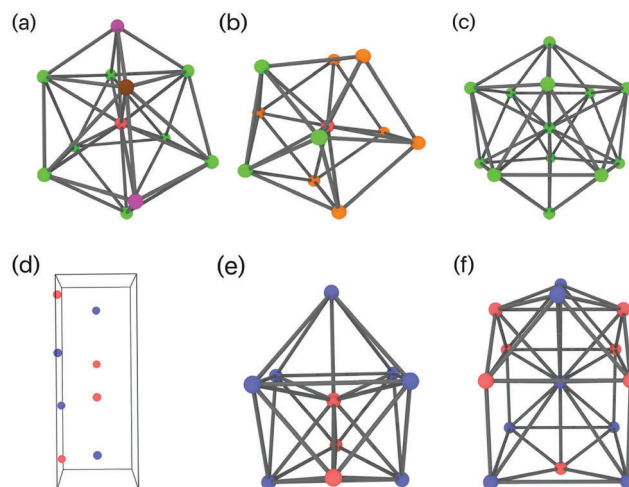

Fig. 4 (a) Z11 motif. The magenta positions display the four-fold symmetry and the brown atom has a six-fold symmetry; (b) mixed motif and the orange positions show the three quadrangles in it; (c) ICO motif; (d) the unit cell of B33 phase; (e) Ni-B33 motif; (f) Zr-B33 motif. The red atoms are Ni and the blues ones are Zr. If one position can be placed with either Ni or Zr, the color is green. The bonds are just plotted for convenience and are not real.

three nearly orthogonal faces. From this perspective, the motif is a combination of ICO and BCC, which is reasonable because B2 is a metastable phase of the system. In the following paragraph, we name it the "Mixed motif" in short.

We note that the stable phase for the $Ni_{50}Zr_{50}$ alloy is B33 and its structure is plotted in Fig. 4(d) where the red atoms are Ni and the blue ones are Zr. Considering the possibility that a crystalline motif may persist in the glassy structure,[32] we extract the Ni-centered (Fig. 4(e)) and Zr-centered (Fig. 4(f)) first-shell structure from the crystalline phase and name them Ni-B33 and Zr-B33 motifs, respectively.

With these four structure motifs together with other common motifs like BCC, FCC, HCP, ICO, 3661,[18,32] Z14, Z15, Z16 (the structure of Z14, Z15, Z16 could be found in ref. 39) as templates, the similarity of each cluster extracted from the atomistic structure of the glass sample to each of the templates is quantified through one-to-one cluster-template alignment analysis.[29–31]

Fig. 5(a) and (b) show the distribution of the alignment score for Ni-centered and Zr-centered clusters in the sub-T_g annealed sample, respectively. The alignment score 0.15 is used as the cutoff[40] to identify the SRO of both the Ni-centered and Zr-centered clusters. For the Ni-centered clusters, three motifs are dominant: Z11, mixed, and Ni-B33 and the peaks in their score distribution are obviously on the left side compared to those of other motifs. Then the fractions of these motifs are calculated to be 18.96%, 15.64%, and 12.68% of the total Ni-centered clusters for Z11, mixed, and Ni-B33 motifs, respectively. We note that in a previous study[21] the dominant SRO around Ni atoms in the $Ni_{50}Zr_{50}$ system was identified to be ICO which is different from our results. The difference would be partially due to different interatomic potentials used in the two simulations. Most likely most of the difference originates from the different templates used in the cluster-template alignment analysis. The new Z11 and mixed SRO motifs revealed by our pairwise-alignment/clique-analysis are missed in the analysis of ref. 21. The B33 crystal motif is also not included in their analysis. Since both Z11 and mixed motifs have large fractions of five-fold symmetry which is prevalent in ICO, in the absence of these two types of templates, many of the mixed and Z11 clusters may have been classified as ICO in the analysis of ref. 21. From this perspective, the pairwise-alignment/clique-analysis method[32] is quite useful in excavating the hidden dominant motifs and these new motifs help us get a clearer picture of the SRO in the $Ni_{50}Zr_{50}$ system. The fraction of ICO in the present work is only 1.68%, which indicates the bad GFA of

the system. As for the Zr-centered motifs, even considering as much as 9 types of motifs, no motif has a fraction more than 4% of the total Zr-centered clusters. In the following, Ni-centered motifs are focused on and we will first look into the chemical order of the three motifs.

In the cluster alignment analysis so far, only geometry is considered without characterizing the types of atoms in each position. Here we adopt a new method to determine not only the whole chemical order of a certain motif, i.e. the average number of Ni atoms and Zr atoms in the motif but also the chemical order in each position of the template. In this new analysis, the clusters which belong to the same SRO motif are overlapped with each other, with the orientation of the clusters in their best alignment score (to the same template) position.[29] Each atomic position in these clusters is labeled with their chemical identity and the chemical order is characterized by the fraction of Zr atoms around each template atom position. The color scheme is the same as that in Fig. 4. First, we take a look at the three motifs in general and find that Zr atoms are rich in Ni-centered clusters with the fraction of more than 0.65 as the dashed lines shown in Fig. 6(b), (d) and (f), which agrees with the results from the pair correlation functions. Then, we investigate the chemical order at each atomic position of the three Ni-centered motifs. For the Z11 motif, the positions 1 and 10 with four-fold symmetry are occupied by less than 15% Zr atoms. These positions could be seen as the traits from the metastable B2 phase when considering the nearby Zr-rich positions and the center of the motif. For position 5 with six-fold symmetry, it's occupied more than 98% Zr atoms. The better chemical order of four- and six-fold symmetry positions lies in that both four- and six-fold symmetries are prevalent in crystals. In this way, the four- and six-fold symmetries can be viewed as traits from crystals and compete with the five-fold symmetry from the amorphous phase. From the mixed motif shown in Fig. 4(b), we hypothesized that it's also a mixture of ICO and the B2 phase. When we look into the chemical order of each position as shown in Fig. 6(c) and (d), there are 4 positions with more than 75% Zr atoms, i.e. 5, 8, 9, 10. From the geometry perspective, we find that 5 and 9, 8 and 9, 9 and 10 form three edges, which are just the intersections of the three quadrangle faces of a B2 unit. The chemical orders of these
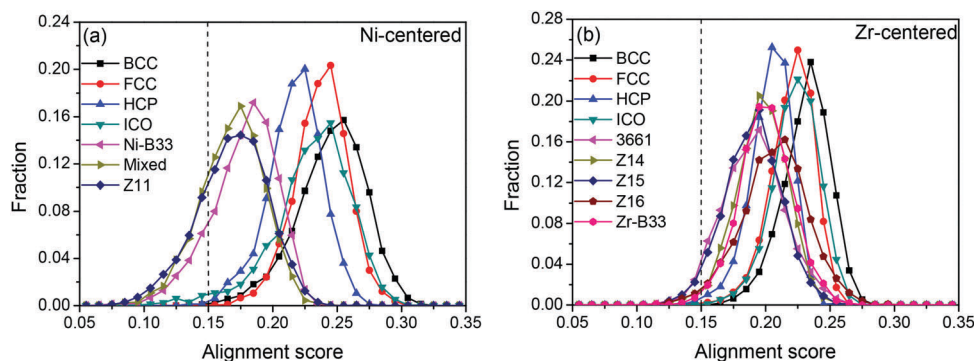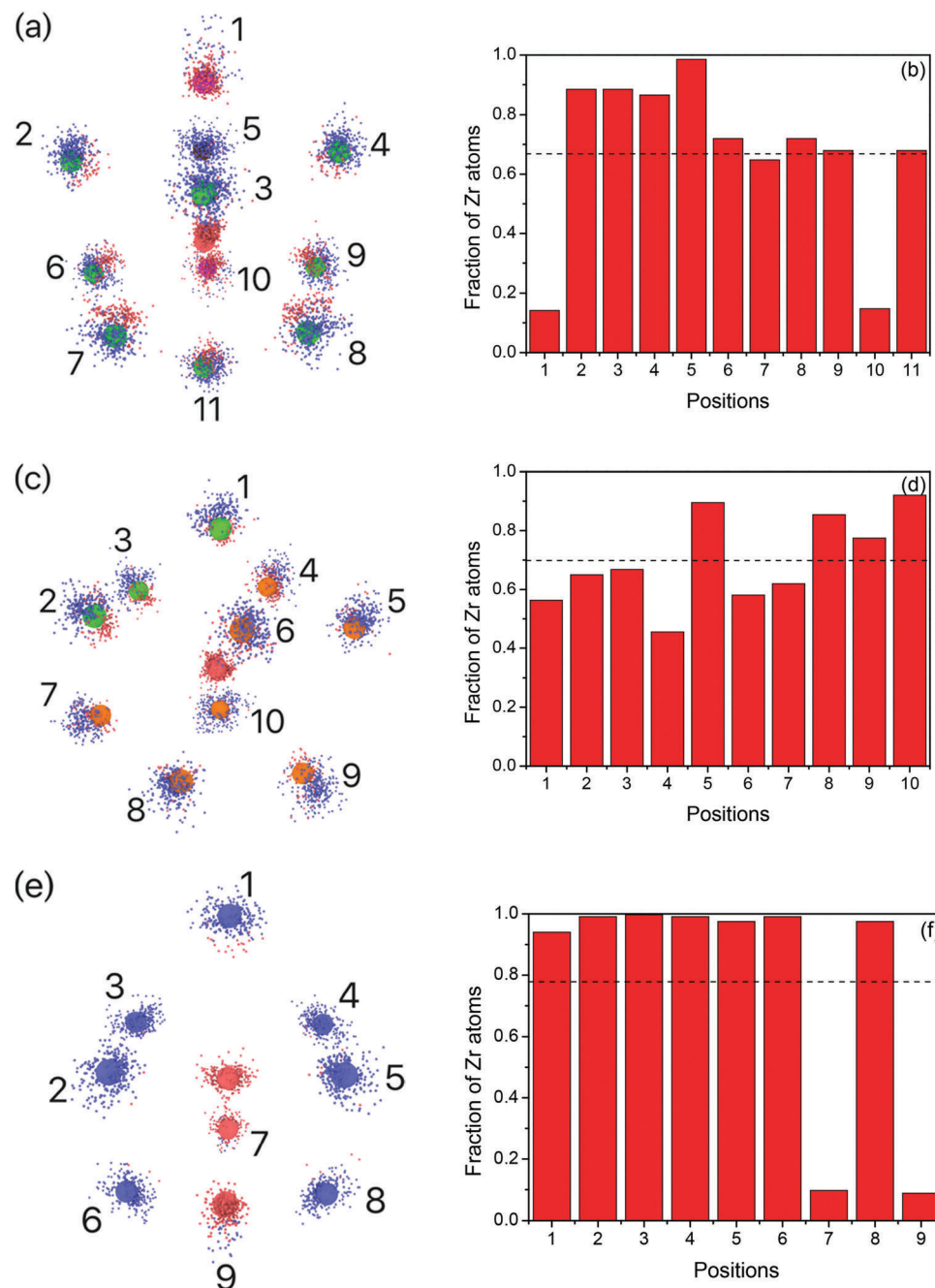

Fig. 5 The distribution of alignment scores of Ni- (a) and Zr-centered clusters (b) in the sub-T_g annealed $Ni_{50}Zr_{50}$ glassy sample at 300 K. The cutoff 0.15 is used to identify both the Ni-centered and Zr-centered motifs.

Fig. 6 The aligned clusters with its template and the fraction of Zr atoms in each position for (a and b): Z11, (c and d): mixed, and (e and f): Ni-B33, respectively. The usage of the colors is the same with Fig. 4 and the dashed lines denote the average composition for each motif.

positions preserve the traits from the B2 phase without much influence from the ICO fragment. As for the Ni-B33 motif (see Fig. 6(e) and (f)), the chemical order at each atomic position matches well with the crystal template, which indicates that the Ni-B33 motif found in this glassy sample is very close to the SRO from the stable crystalline phase. The Ni-B33 crystalline and the few ICO motifs contribute together to the marginal GFA of the system. The chemical order and the structure of the motif are connected firmly here. On the one hand, the structure could determine the chemical order of each position to

some degree. If there is crystalline geometry persisting in the motif, like the parts of the B2 phase in the mixed motif, some positions in these crystalline traits would display decent chemical order as shown by the positions 5, 8, 9, and 10. On the other hand, chemical order could also influence the structure of the motif because of the different bond lengths between atoms. The chemical order in each position plays a key role in determining the distance between the position and the motif center. Besides, chemical order could have an impact on the symmetry. As seen in the Z11 motif, the chemical order of

four-fold symmetry varies significantly from that of five-fold symmetry. In this light, chemical order and structure are mutually interacted with each other.

3.4. The evolution of structural order

Having demonstrated the geometry and chemical order of the three Ni-centered motifs, we then study the change in the fraction of these motifs with cooling rate, temperature, and time in the process of sub-T_g annealing. Fig. 7(a) shows the fractions of the Ni-centered motifs at different effective cooling rates. There is an increasing trend for Z11, mixed, and Ni-B33 motifs with decreasing effective cooling rates, which is reasonable because the structure has more time to relax and form better SROs. Among these three motifs, we find that Ni-B33 displays the sharpest increase from about 9% at 10^{13} K s^{-1} to around 13% in the sub-T_g annealed sample. The ICO, however, almost remains at the same level of less than 2% of the total Ni centered clusters. In experiment, the cooling rate is normally slower than 10^6 K s^{-1} and the fraction of Ni-B33 crystalline motifs would be significant in the experimental samples based on the trend from our MD simulations. The development of the B33 order will hinder the formation of BMG. To investigate the evolution of SROs as the function of temperature, Fig. 7(b) plots the fractions of different motifs at various temperatures at 10^{10} K s^{-1} cooling rate. With decreasing temperatures, both the glass-forming motifs and the Ni-B33 motifs show a tendency to increase. Both the glass-forming and the crystalline B33 motifs start to develop rapidly as soon as the temperature is lower than 1300 K until the system reaches the

glass transition temperature. While the fraction of the Ni-B33 crystalline motifs increases almost linearly between 1300 K and T_g and continues to grow even below T_g, the most increase in the fractions of the Z11 and mixed clusters occurs from about 1000 K to 800 K, which is near T_g. We also investigate the time evolution of these SROs during sub-T_g annealing at 800 K for 2000 ns. Fig. 7(c) plots the fractions of Z11, mixed and Ni-B33 motifs at different sub-T_g annealing times. The samples are chosen every 200 ns and the inherent structures are used for the analysis. To get more reliable statistics, samples 5 ns before and after the selected time are also used to calculate the average and the error bars. From 0 to 600 ns, the fraction of the Ni-B33 motif increases with the slight decrease of Z11 and mixed motifs. Then, the glass-forming motifs increase constantly with the decrease and level off of the Ni-B33 motifs from 600 ns to 1200 ns. In the latter time, the fraction of the mixed motif decreases while that of the Z11 motif increases. It seems that the fluctuation causes some interchange between the mixed and Z11 motifs, which is also seen in Fig. 7(b) below the glass transition temperature. Through the whole process, the number of glass-forming motifs competes with the crystalline B33 motifs and there's also an exchange between the glass-forming motifs. The total fraction of all the three dominant SROs increases with annealing time as shown in Fig. 7(d) which explains the decreasing potential energy during sub-T_g annealing.

The snapshots of some typical structures at high and low temperatures are shown in Fig. 8. Fig. 8(a)–(c) are the snapshots at 1600 K and Fig. 8(d)–(f) are those at 300 K. In Fig. 8(a), (b), (d) and (e), the red ball represents Ni and the blue one stands
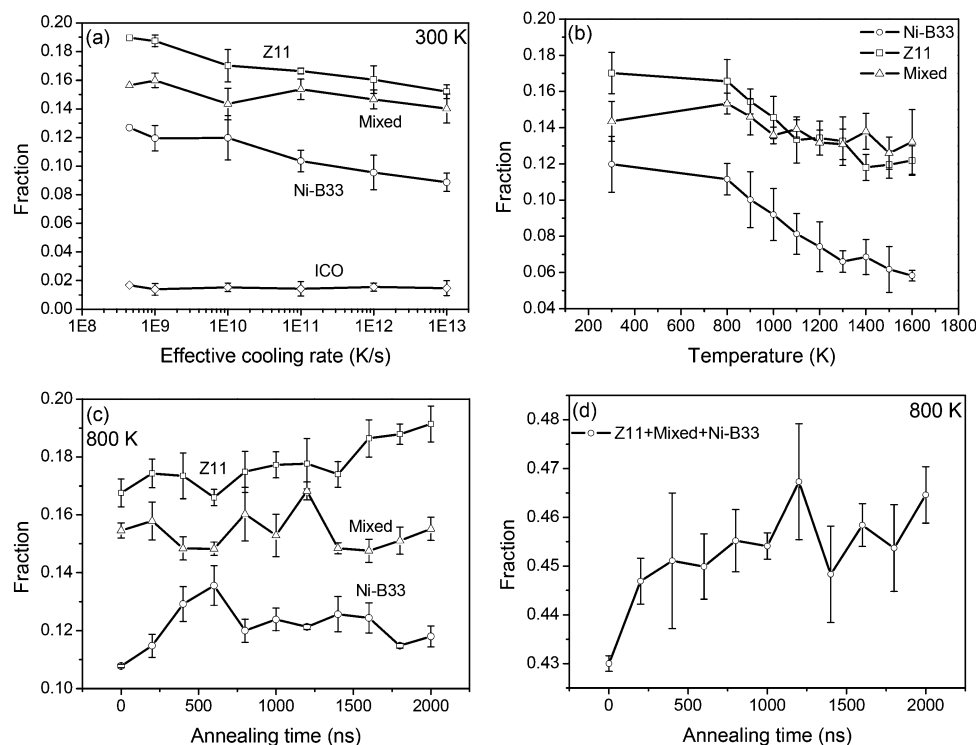

Fig. 7 (a) The change of the fractions of different Ni-centered motifs at 300 K with effective cooling rates; (b) fractions of Ni-centered B33 motifs and the glass-forming motifs, Z11 and mixed, at various temperatures at 10^{10} K s^{-1} cooling rate; (c) the fractions of different motifs during the sub-T_g annealing process at 800 K; (d) the total fraction of the dominant Ni-centered short-range orders in the sub-T_g annealing process at 800 K.

for Zr. If two atoms are within the cutoff distance determined by the first minimum of the corresponding partial $g(r)$, there is a bond connecting them. Fig. 8(a) and (d) show the configurations of atoms. Not much difference can be seen from the snapshots of all the atoms at 1600 K and 300 K. However, when only the Ni-B33 clusters are plotted as shown in Fig. 8(b) and (e) respectively, we can see that the number of Ni-B33 motifs grows significantly and they become more connected with each other when the temperature is lowered. In order to see the relationship between the three types of dominant Ni-centered clusters (*i.e.*, Z11, mixed, and Ni-B33), the spatial distribution of the center atoms of these clusters are also shown in Fig. 8(c) and (f) for 1600 K and 300 K respectively. In these plots, if the two centers are within the distance of 3 Å, there is a bond connecting them. The red one represents the center of the mixed motif, the green one stands for the Z11 center, and the blue one for the Ni-B33 motif center. With the decrease of temperature, there are more dominant motifs in the system and they become more interconnected with each other.
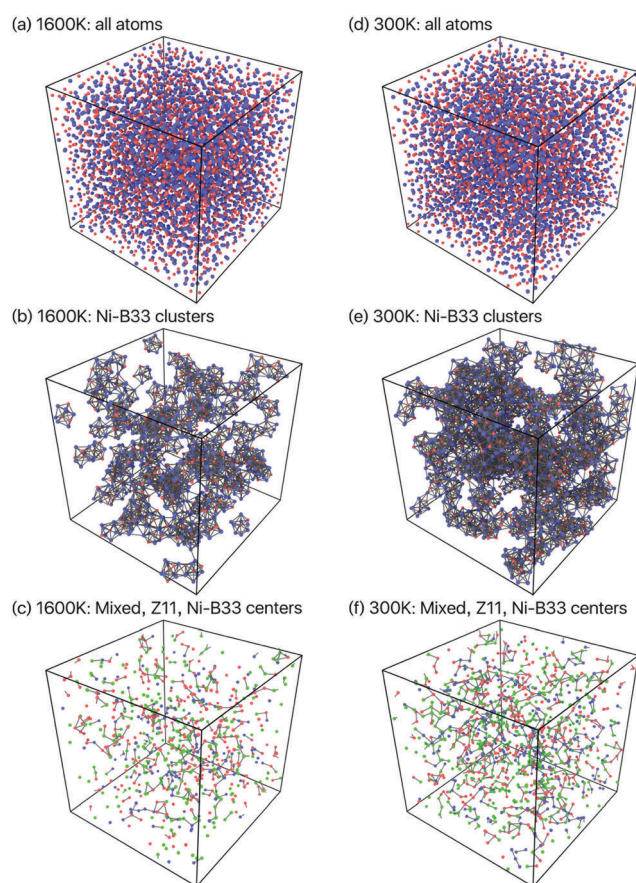
Fig. 8 (a–c) and (d–f) are snapshots at 1600 K and 300 K, respectively. In (a and b) and (d and e), the red one represents Ni and the blue one for Zr. If two atoms are within the cutoff distance determined by the first minimum of the corresponding partial $g(r)$, there is a bond connecting them. (a and d) are the configurations including all the atoms, (b and e) plot the Ni-B33 clusters. In (c and f), only the centers of the dominant Ni-centered motifs are shown. The red one represents the center of the mixed motif, the green one stands for the Z11 center, and the blue one is the Ni-B33 center. If the two centers are within the distance of 3 Å, there is a bond connecting them.

3.5. Connection between structure and dynamics

Our long time sub-T_g annealing simulation also provides useful atomistic trajectories to study the relationship between structure and dynamics during the glass formation process. The dynamics of a system is usually quantified with mean-square displacements (MSD) as a function of time:

$$\langle R^2(t) \rangle = \frac{1}{N} \left\langle \sum_{i=1}^{N} |\boldsymbol{R}_i(t + \tau) - \boldsymbol{R}_i(\tau)|^2 \right\rangle \qquad (4)$$

where N is the number of atoms, R_i are the coordinates of atom i, and τ is the arbitrary origin of time. The typical MSD as the function of time for Ni and Zr atoms at 800 K is shown in Fig. 9(a). However, since the atomistic structures in the undercooled liquids are dynamically changing, we need to choose a proper time window (Δt) so that the mobility of each atom and its structural character can be simultaneously determined in order to quantify the relationship between structure and dynamics.[41] Here, we use the similar method to that in ref. 8 to determine Δt which is 5 ns for the present system. As one can see from Fig. 9(a), the MSD for Ni atoms at a time interval of 5 ns is only 2.34 Å^2 which is equal to 1.53 Å in terms of mean displacements. Considering the first peak of Ni–Ni $g(r)$ at around 2.56 Å, we believe that the atomistic structure changing within the time window of 5 ns could be negligible so that the mobility of the atoms at a given structure and the relationship between structure and dynamics can be characterized. We then calculate the self-part of the time-dependent van Hove correlation function[42] with Δt = 5 ns and the function is defined as:

$$G_S(r, t) = \frac{1}{N} \left\langle \sum_{j=1}^{N} \delta\left(r + r_j(0) - r_j(t)\right) \right\rangle \qquad (5)$$

Fig. 9(b) displays the van Hove correlation function at 800 K with Δt = 5 ns. A cutoff of 1.44 Å is chosen to divide the Ni atoms into two groups: (1) immobile atoms whose displacements are less than the cutoff distance for the time window; (2) mobile atoms on the right side of the cutoff which move relatively faster as if they are still in the liquid state. In Fig. 9(c), the fraction of mobile Ni atoms (*i.e.*, number of mobile Ni atoms over all Ni atoms) as the function of annealing time at 800 K is given which shows that the fraction of mobile Ni atoms decreases with annealing time. The sub-T_g annealing, which helps lower the potential energy of the samples, simultaneously slows down the dynamics of the system. We also studied the mobility of the Ni center atom in each SRO motif. The fractions of the mobile atoms in different SRO motif centers are plotted in Fig. 9(d) in comparison with that of Ni atoms in the whole sample. In some glass-forming undercooled liquids, Cheng *et al.*[43,44] reported that ICO is the microscopic structural origin of the dynamical slowdown in Cu–Zr and Cu–Zr–Al systems. From Fig. 9(d), we can see that the fraction of the mobile atoms is lower for the center atoms of Z11, mixed, and Ni-B33 motifs as compared to that of the overall Ni atoms in the sample. In this regard, the developing SROs in the annealing process form a more sluggish state with lower energy, which is a reasonable explanation for the more stable
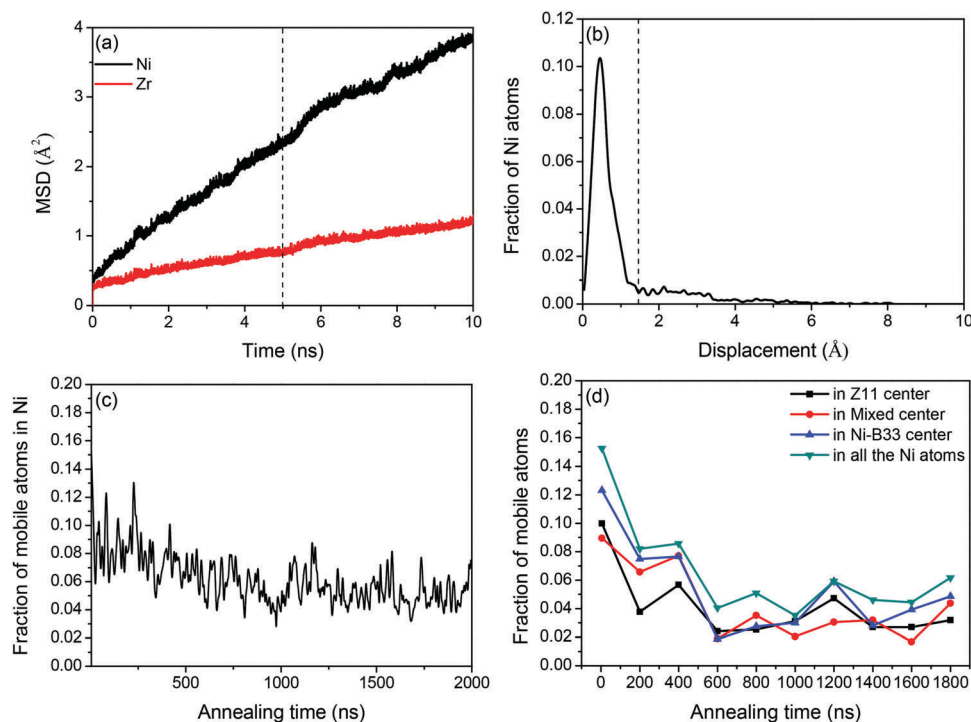
Fig. 9 (a) The mean–square displacement (MSD) in the first 10 ns of the sub-T_g annealing process. At the time of 5 ns, the MSD is only 2.34 Å^2 which is equal to 1.53 Å mean displacement. (b) Van-hove correlation at the beginning of sub-T_g annealing and the multiple small peaks indicate the existence of hopping processes. The cutoff is chosen at 1.44 Å to distinguish the mobile and immobile atoms. (c) The fraction of mobile atoms in Ni at different annealing times. (d) The fraction of mobile atoms in Z11, mixed, Ni-B33 center, and all the Ni atoms through the annealing process.

and relaxed glassy sample achieved using the sub-T_g annealing method. The development of SRO structures here determines the dynamic properties and the potential energy. Thus, the structure and the dynamics are strongly correlated with each other.

4. Conclusions

In the present work, we performed a MD study on the marginal glass-forming Ni$_{50}$Zr$_{50}$ system with the newly developed EAM potential. After determining the glass transition temperature of around 850 K, we carry out sub-T_g annealing at 800 K for 2.0 μs and then quench to 300 K to obtain a well-relaxed glassy sample. From the results of the potential energy, pair correlation functions and structure factor analysis, enhanced short-to-medium range orders are observed in the atomistic structure from the long time sub-T_g annealed sample. Then the state-of-the-art structural analysis algorithms based on cluster alignment and pair-wise alignment methods are applied to characterize and investigate SROs. Two dominant glass-forming motifs are excavated from the pair-wise alignment method and the fraction of the Ni-centered B33 crystalline motif is also found to be at the same level as the two dominant glass-forming motifs. The ICO motif, however, is less than 2% of the total Ni centered clusters. Chemical orders in the dominant SRO motif are also determined based on the cluster alignment method. In the sense of chemical order, the traits of the B2 phase are found in the glass-forming motifs and the

Ni-centered B33 motif has a nearly perfect chemical order as that in the crystalline phase. The few ICO motifs and the large fraction of the crystalline Ni-B33 motif contribute together to the marginal GFA of this system. We also study the evolution of the dominant Ni-centered SROs with cooling rates, temperatures and time (for sub-T_g annealing sample). It is found that SROs are enhanced with decreasing cooling rates and by sub-T_g annealing. In the annealing process, the competition between the glass-forming motifs and the crystalline ones is observed and the increasing SROs are accompanied with decreasing potential energy and more sluggish dynamics.

Conflicts of interest

There are no conflicts of interest to declare.

Acknowledgements

References

1 D. H. Xu, B. Lohwongwatana, G. Duan, W. L. Johnson and C. Garland, *Acta Mater.*, 2004, **52**, 2621–2624.

2 D. Wang, Y. Li, B. B. Sun, M. L. Sui, K. Lu and E. Ma, *Appl. Phys. Lett.*, 2004, **84**, 4029–4031.

3 Y. Li, Q. Guo, J. A. Kalb and C. V. Thompson, *Science*, 2008, **322**, 1816–1819.

4 A. Inoue and W. Zhang, *Mater. Trans.*, 2004, **45**, 584–587.

5 M. B. Tang, D. Q. Zhao, M. X. Pan and W. H. Wang, *Chin. Phys. Lett.*, 2004, **21**, 901–903.

6 G. Duan, D. H. Xu, Q. Zhang, G. Y. Zhang, T. Cagin, W. L. Johnson and W. A. Goddard III, *Phys. Rev. B: Condens. Matter Mater. Phys.*, 2005, **71**, 224208.

7 Y. Zhang, C. Z. Wang, M. I. Mendelev, F. Zhang, M. J. Kramer and K. M. Ho, *Phys. Rev. B: Condens. Matter Mater. Phys.*, 2015, **91**, 180201(R).

8 Y. Zhang, C. Z. Wang, F. Zhang, M. I. Mendelev, M. J. Kramer and K. M. Ho, *Appl. Phys. Lett.*, 2014, **105**, 151910.

9 M. Lee, C. M. Lee, K. R. Lee, E. Ma and J. C. Lee, *Acta Mater.*, 2011, **59**, 159–170.

10 J. M. López, J. A. Alonso and L. J. Gallego, *Phys. Rev. B: Condens. Matter Mater. Phys.*, 1987, **36**, 3716–3722.

11 M. H. Yang, S. N. Li, Y. Li, J. H. Li and B. X. Liu, *Phys. Chem. Chem. Phys.*, 2015, **17**, 13355–13365.

12 A. W. Weeber and H. Bakker, *J. Phys. F: Met. Phys.*, 1988, **18**, 1359–1369.

13 Z. Altounian and J. O. Strom-Olsen, *Phys. Rev. B: Condens. Matter Mater. Phys.*, 1983, **27**, 4149–4156.

14 R. Ray, B. C. Giessen and N. J. Grant, *Scr. Metall.*, 1968, **2**, 357–359.

15 W. K. Luo, H. W. Sheng, F. M. Alamgir, J. M. Bai, J. H. He and E. Ma, *Phys. Rev. Lett.*, 2004, **92**, 145502.

16 Y. Q. Cheng, E. Ma and H. W. Sheng, *Phys. Rev. Lett.*, 2009, **102**, 245501.

17 H. W. Sheng, W. K. Luo, F. M. Alamgir, J. M. Bai and E. Ma, *Nature*, 2006, **439**, 419–425.

18 Y. Sun, Y. Zhang, F. Zhang, Z. Ye, Z. J. Ding, C. Z. Wang and K. M. Ho, *J. Appl. Phys.*, 2016, **120**, 015901.

19 H. K. Kim, M. Lee, K. R. Lee and J. C. Lee, *Acta Mater.*, 2013, **61**, 6597–6608.

20 N. Wang, C. R. Li, Z. M. Du and F. G. Wang, *Calphad*, 2007, **31**, 413–421.

21 M. H. Yang, J. H. Li and B. X. Liu, *RSC Adv.*, 2017, **7**, 18358–18365.

22 S. R. Wilson and M. I. Mendelev, *Philos. Mag.*, 2015, **95**, 224–241.

23 M. W. Finnis and J. E. Sinclair, *Philos. Mag. A*, 1984, **50**, 45–55.

24 P. G. Debenedetti and F. H. Stillinger, *Nature*, 2001, **410**, 259–267.

25 M. J. Kramer, H. Mecco, K. W. Dennis, E. Vargonova, R. W. McCallum and R. E. Napolitano, *J. Non-Cryst. Solids*, 2007, **353**, 3633–3639.

26 M. P. Allen and D. J. Tildesley, *Computational Simulation of Liquids*, Clarendon Press, 1991.

27 F. Zhang, M. I. Mendelev, Y. Zhang, C. Z. Wang, M. J. Kramer and K. M. Ho, *Appl. Phys. Lett.*, 2014, **104**, 061905.

28 Y. Zhang, F. Zhang, C. Z. Wang, M. I. Mendelev, M. J. Kramer and K. M. Ho, *Phys. Rev. B: Condens. Matter Mater. Phys.*, 2015, **91**, 064105.

29 X. W. Fang, C. Z. Wang, Y. X. Yao, Z. J. Ding and K. M. Ho, *Phys. Rev. B: Condens. Matter Mater. Phys.*, 2010, **82**, 184204.

30 X. W. Fang, L. Huang, C. Z. Wang, K. M. Ho and Z. J. Ding, *J. Appl. Phys.*, 2014, **115**, 053522.

31 X. W. Fang, C. Z. Wang, S. G. Hao, M. J. Kramer, Y. X. Yao, M. I. Mendelev, Z. J. Ding, R. E. Napolitano and K. M. Ho, *Sci. Rep.*, 2011, **1**, 194.

32 Y. Sun, F. Zhang, Z. Ye, Y. Zhang, X. W. Fang, Z. J. Ding, C. Z. Wang, M. I. Mendelev, R. T. Ott, M. J. Kramer and K. M. Ho, *Sci. Rep.*, 2016, **6**, 23734.

33 S. Plimpton, *J. Comput. Phys.*, 1995, **117**, 1–19.

34 Y. X. Huang, L. Huang, C. Z. Wang, M. J. Kramer and K. M. Ho, *J. Appl. Phys.*, 2015, **118**, 195902.

35 L. Huang, C. Z. Wang, S. G. Hao, M. J. Kramer and K. M. Ho, *Phys. Rev. B: Condens. Matter Mater. Phys.*, 2010, **81**, 014108.

36 I. Bakonyi, *Acta Mater.*, 2005, **53**, 2509–2520.

37 J. L. Finney, *Proc. R. Soc. A*, 1970, **319**, 479–493.

38 J. L. Finney, *Nature*, 1977, **266**, 309–314.

39 Y. Q. Cheng and E. Ma, *Prog. Mater. Sci.*, 2011, **56**, 379–473.

40 Y. Zhang, R. Ashcraft, M. I. Mendelev, C. Z. Wang and K. F. Kelton, *J. Chem. Phys.*, 2016, **145**, 204505.

41 M. C. C. Ribeiro, *Phys. Chem. Chem. Phys.*, 2004, **6**, 771–774.

42 L. V. Hove, *Phys. Rev.*, 1954, **95**, 249–262.

43 Y. Q. Cheng, E. Ma and H. W. Sheng, *Appl. Phys. Lett.*, 2008, **93**, 111913.

44 Y. Q. Cheng, H. W. Sheng and E. Ma, *Phys. Rev. B: Condens. Matter Mater. Phys.*, 2008, **78**, 014207.